European Journal of Mechanics B/Fluids 49 (2015) 77–88

Contents lists available at ScienceDirect

European Journal of Mechanics B/Fluids

journal homepage: www.elsevier.com/locate/ejmflu

Two-dimensional Kelvin–Helmholtz instabilities of multi-component fluids

Hyun Geun Lee [a], Junseok Kim [b,*]

[a] Institute of Mathematical Sciences, Ewha Womans University, Seoul 120-750, Republic of Korea
[b] Department of Mathematics, Korea University, Seoul 136-713, Republic of Korea

HIGHLIGHTS

- The Kelvin–Helmholtz instability of multi-component (more than two) fluids is studied numerically.
- The instability is governed by the modified Navier–Stokes equations and the multi-component convective Cahn–Hilliard equations.
- We investigate the effects of surface tension, density ratio, magnitude of velocity difference, and forcing.

ARTICLE INFO

Article history:
Received 17 May 2014
Received in revised form
8 August 2014
Accepted 16 August 2014
Available online 27 August 2014

Keywords:
Kelvin–Helmholtz instability
Multi-component fluid flows
Phase-field model
Linear growth rate
Billowing cloud formation

ABSTRACT

The Kelvin–Helmholtz instability of multi-component (more than two) incompressible and immiscible fluids is studied numerically using a phase-field model. The instability is governed by the modified Navier–Stokes equations and the multi-component convective Cahn–Hilliard equations. A finite difference method is used to discretize the governing system. To solve the equations efficiently and accurately, we employ the Chorin's projection method for the modified Navier–Stokes equations and the recently developed practically unconditionally stable method for the multi-component Cahn–Hilliard equations. Through our model and numerical solution, we investigate the effects of surface tension, density ratio, magnitude of velocity difference, and forcing on the Kelvin–Helmholtz instability of multi-component fluids. It is shown that increasing the surface tension or the density ratio reduces the growth of the Kelvin–Helmholtz instability. And it is also observed that as the initial horizontal velocity difference gets larger, the interface rolls up more. We also found that the billow height reaches its maximum more slowly as the initial wave amplitude gets smaller. And, for the linear growth rate for the Kelvin–Helmholtz instability of two-component fluids, the simulation results agree well with the analytical results. From comparison between the numerical growth rate of two- and three-component fluids, we observe that the inclusion of extra layers can alter the growth rate for the Kelvin–Helmholtz instability. Finally, we simulate the billowing cloud formation which is a classic example of the Kelvin–Helmholtz instability and cannot be seen in binary fluids. With our multi-component method, the details of the real flow (e.g., the asymmetry in the roll-up and the self-interaction of the shear layer) are well captured.

© 2014 Elsevier Masson SAS. All rights reserved.

1. Introduction

When there is a sufficiently large velocity difference (e.g., shear flow) across a small amplitude perturbed interface between two fluids, the interface is unstable. This interfacial instability is known as the Kelvin–Helmholtz (KH) instability. The instability occurs when the destabilizing effect of shear across the interface overcomes the stabilizing effect of gravity and/or surface tension. It can be observed in a wide variety of natural situations. A classic example is the spectacular billowing cloud formation in the lower atmosphere, an occurrence which is often associated with atmospheric turbulence [1]. It was suggested that the KH instability may provide a trigger mechanism for pulsar glitches [2].

The classical version of the KH instability is outlined by Kelvin [3] and Helmholtz [4], and the associated linear stability has been investigated analytically by Taylor [5] and Miles [6] and numerically by Hazel [7]. The nonlinear development of the KH instability has been extensively investigated experimentally [8,9] and numerically [10–32]. Numerical studies dealt mainly with the

* Corresponding author. Tel.: +82 2 3290 3077; fax: +82 2 929 8562.
E-mail addresses: cfdkim@korea.ac.kr, junseok_kim@yahoo.com (J. Kim).
URL: http://math.korea.ac.kr/~cfdkim (J. Kim).

http://dx.doi.org/10.1016/j.euromechflu.2014.08.001
0997-7546/© 2014 Elsevier Masson SAS. All rights reserved.

KH instability at the interface of a two-phase system. Rangel and Sirignano [10] used the vortex-sheet discretization approach to investigate the effects of surface tension and density ratio on the nonlinear evolution of initially small disturbances at an interface between two fluids neglecting the gravitational force. They showed that increasing the surface tension or the density ratio reduces the growth of the disturbance. Numerical simulations of three-dimensional temporally evolving plane mixing layers were performed by Rogers and Moser [12]. They found that the spanwise vorticity rolls up into a corrugated spanwise roller and the streamwise rib vortices develop in the braid region between the rollers. Zhang et al. [18] studied the effects of surface tension on the two-dimensional KH instability of density-matched fluids using a lattice Boltzmann multi-phase model [33] in the nearly incompressible limit and reported that their results are in good agreement with those of Rogers and Moser [12]. Tauber et al. [20] investigated the effects of density ratio, Reynolds number, and Weber number on the nonlinear behavior of a sheared immiscible fluid interface using the front-tracking method. They showed that high enough Reynolds and relatively low Weber numbers lead to the generation of fingers of interpenetrating fluids. Using a fully adaptive nonstiff strategy based on the immersed boundary method, Ceniceros and Roma [22] presented a numerical investigation of the long-time dynamics of two immiscible density- and viscosity-matched fluids shearing past one another. Sahu et al. [24] studied the pressure-driven displacement of a highly viscous fluid by a less viscous one and their results demonstrated that the development of the KH instability becomes more pronounced with increasing viscosity ratio, Reynolds and Schmidt numbers, leading to more intense mixing and rapid removal of the more viscous fluid. The authors [25] also studied the pressure-driven miscible displacement flow in tilted channels with density contrasts at moderate to large Reynolds numbers. Their results indicated that the rates of mixing and displacement are enhanced with increasing density ratio, Froude number, and inclination angle. Computational investigations of the miscible displacement flow are also presented in [34,35]. Sohn et al. [27] performed long-time simulations of the KH instability using an adaptive vortex method and their results showed that the KH instability evolves a secondary instability at a late time, distorting the internal rollup, and eventually develops to a disordered structure. Shadloo and Yildiz [28] examined the effects of Richardson number and density ratio on the development of the KH instability of two incompressible, immiscible, and inviscid fluids using a smoothed particle hydrodynamics method [36] and observed that the growth rate of the KH instability is mainly controlled by the value of the Richardson number, not by the nature of the stabilizing forces. Redapangu et al. investigated the pressure-driven displacement flow of two immiscible fluids of different densities and viscosities in two- [30] and three- [31] dimensional channels. They found that the flow is relatively more coherent in a three-dimensional channel than that in a two-dimensional channel and screw-type instabilities were seen in a three-dimensional channel those cannot be observed in a two-dimensional channel. Fakhari and Lee [32] applied a multiple-relaxation-time lattice Boltzmann method to simulate the KH instability of immiscible two-phase fluids at high Reynolds numbers. They found that increasing the Reynolds number results in a more chaotic interface evolution and eventually shattering of the interface, while surface tension is shown to have a stabilizing effect. For more details on instabilities, we refer to a recent review by Govindarajan and Sahu [37].

Although the basic nonlinear behavior of the KH instability at the interface of a two-phase system has been extensively studied, the understanding of the KH instability of multi-component (more than two) fluids is still quite limited due to the complexity of the interfacial dynamics and the numerical implementation. This paper presents, for the first time to the authors' knowledge, numerical simulations of the KH instability of multi-component fluids. We are particularly interested in simulating the billowing cloud formation and evaluating the effects of surface tension, density ratio, magnitude of velocity difference, and forcing on the KH instability using a phase-field model [38]. The advantages of the phase-field method are: (1) An explicit tracking of the interface is unnecessary. (2) Topological changes are automatically handled. (3) A time step can be chosen larger than the time step used in the traditional lattice Boltzmann methods which are explicit in nature. (4) A potential disadvantage of the lattice Boltzmann method is that because of its formulation it allows finite compressibility of the fluid. However, we may treat quasi-incompressible systems [39]. Therefore, the phase-field method can also be applied to model double emulsions [40,41], multi-film flow [42], and multi-layer coating. In the phase-field model, the fluid dynamics is governed by the modified Navier–Stokes equations and the multi-component convective Cahn–Hilliard (CH) equations [43,44]. We discretize the governing system using a finite difference method. To solve the equations efficiently and accurately, we employ Chorin's projection method [45] for the modified Navier–Stokes equations and the recently developed practically unconditionally stable method for the multi-component CH equations [44].

The paper is organized as follows. In Section 2, we present the governing equations that describe the flow of N incompressible immiscible fluids, and state the underlying physics and all assumptions that have been made. In Section 3, the problem description for the KH instability of multi-component fluids is provided. In Section 4, a numerical solution is given. We perform some characteristic numerical experiments for the KH instability of multi-component fluids in Section 5. Finally, conclusions are drawn in Section 6.

2. Phase-field model for the mixture of N incompressible immiscible fluids

We consider the flow of N incompressible immiscible fluids. Let $\mathbf{c} = (c_1, c_2, \ldots, c_N)$ be a vector-valued phase-field, where each order parameter c_k is the concentration of each component in the mixture. Thus, admissible states will belong to the Gibbs N-simplex

$$G := \left\{ \mathbf{c} \in \mathbb{R}^N \;\middle|\; \sum_{k=1}^{N} c_k = 1,\ 0 \le c_k \le 1 \right\}. \tag{1}$$

The free energy of a multi-component system can be written as follows [46]:

$$\mathcal{F}(\mathbf{c}) = \int_{\Omega} \left(F(\mathbf{c}) - \sum_{i<j}^{N} \epsilon_{ij}^2 \nabla c_i \cdot \nabla c_j \right) d\mathbf{x},$$

where Ω is a bounded open subset of $\mathbb{R}^d$ ($d = 1, 2, 3$) occupied by the system, $F(\mathbf{c})$ is the Helmholtz free energy density, and $\epsilon_{ij} > 0$ is a parameter that takes into account the molecular interactions between components i and j. By assuming that $\epsilon_{ij} = \epsilon$ for all $i < j$, the total free energy $\mathcal{F}(\mathbf{c})$ becomes

$$\mathcal{F}(\mathbf{c}) = \int_{\Omega} \left(F(\mathbf{c}) + \frac{\epsilon^2}{2} \sum_{k=1}^{N} |\nabla c_k|^2 \right) d\mathbf{x}.$$

Here, we take $F(\mathbf{c}) = 0.25 \sum_{k=1}^{N} c_k^2 (1 - c_k)^2$. The surface tensions σ_{ij} between phases i and j will be considered in the modified Navier–Stokes equations (not in the total free energy $\mathcal{F}(\mathbf{c})$). This consideration gives that all interfaces have a uniform thickness. The time evolution of $\mathbf{c}$ is governed by the gradient of the energy with respect to the $\dot{H}^{-1}$ inner product under the additional

constraint (1). This constraint has to hold everywhere at all times. In order to ensure the last constraint, we use a Lagrange multiplier β_k [43,44,46–50]. The temporal evolution of c_k is given by the following convective CH equation: for $k = 1, 2, \ldots, N$,

$$\frac{\partial c_k}{\partial t} + \nabla \cdot (c_k \mathbf{u}) = \nabla \cdot (M(\mathbf{c}) \nabla \mu_k), \tag{2}$$

$$\mu_k = f(c_k) - \epsilon^2 \Delta c_k + \beta_k, \tag{3}$$

where $\mathbf{u} = (u, v)$ is the fluid velocity, $M(\mathbf{c})$ is a mobility, $f(c_k) = c_k(c_k - 0.5)(c_k - 1)$, and $\beta_k = -c_k \sum_{j=1}^{N} f(c_j)$ [49]. Cahn and Hilliard [51] used the mobility rather than the molecular diffusion coefficient [52]. The mobility is treated as a concentration dependent mobility in [53–59] (e.g., $M(\mathbf{c}) = \sum_{i<j}^{N} c_i c_j$ for a multicomponent system), and the CH equation has been extensively employed with a constant mobility [60–66]. In this paper, we take the mobility to be constant ($M(\mathbf{c}) \equiv M$), as a concentration dependent mobility is computationally more expensive. The mobility M controls the relaxation time of the interface [67], and has to be chosen judiciously. Jacqmin [68] summarized the physical considerations that should go into choosing an interfacial relaxation time: "straining flows can thin or thicken the interface and this must be resisted by a high enough diffusion. On the other hand, too large a diffusion will overly damp the flow".

The characteristics of multiphase fluid flow is investigated by coupling the modified Navier–Stokes equations and Eqs. (2)–(3) with the constant mobility M:

$$\rho(\mathbf{c}) \left(\frac{\partial \mathbf{u}}{\partial t} + \mathbf{u} \cdot \nabla \mathbf{u} \right) = -\nabla p + \nabla \cdot \left[\eta(\mathbf{c}) (\nabla \mathbf{u} + \nabla \mathbf{u}^{\mathrm{T}}) \right] + \mathbf{SF}(\mathbf{c}) + \rho(\mathbf{c}) \mathbf{g}, \tag{4}$$

$$\nabla \cdot \mathbf{u} = 0, \tag{5}$$

$$\frac{\partial c_k}{\partial t} + \nabla \cdot (c_k \mathbf{u}) = M \Delta \mu_k, \tag{6}$$

$$\mu_k = f(c_k) - \epsilon^2 \Delta c_k + \beta_k, \tag{7}$$

where $\rho(\mathbf{c})$ is the variable density, p is the pressure, $\eta(\mathbf{c})$ is the variable viscosity, $\mathbf{SF}(\mathbf{c})$ is the surface tension force, and $\mathbf{g} = (0, -g)$ is the gravity term under gravitational acceleration g. $\rho(\mathbf{c})$ and $\eta(\mathbf{c})$ are defined as $\rho(\mathbf{c}) = \sum_{k=1}^{N} \rho_k c_k$ and $\eta(\mathbf{c}) = \sum_{k=1}^{N} \eta_k c_k$, where ρ_k and η_k are the density and viscosity of the kth fluid, respectively. For a large density ratio, the continuity equation cannot be reduced to Eq. (5). In such cases, we should use $\rho_t + \nabla \cdot (\rho \mathbf{u}) = 0$ as the continuity equation. The surface tension is not additive [69] and is dependent on the potential energy related to the interaction of a pair of different molecules [70]. This dependence can be ignored in the heuristic models for the surface tension that are widely used. Here, for $\mathbf{SF}(\mathbf{c})$ in Eq. (4), we use the generalized continuous surface tension force formulation [43]: $\mathbf{SF}(\mathbf{c}) = \sum_{i=1}^{N-1} \left(\sum_{j=i+1}^{N} 0.5 \sigma_{ij} [\mathbf{sf}(c_i) + \mathbf{sf}(c_j)] \delta(c_i, c_j) \right)$, where σ_{ij} is the physical surface tension coefficient between fluids i and j, $\mathbf{sf}(c_i) = -6\sqrt{2}\epsilon \nabla \cdot (\nabla c_i / |\nabla c_i|) |\nabla c_i| \nabla c_i$, and $\delta(c_i, c_j) = 5 c_i c_j$.

3. Definition of the problem

The KH instability can occur at the interface between N horizontal parallel fluids with different velocities and densities. To simulate this natural flow phenomenon, we consider the flow of N incompressible and immiscible fluids that are bounded by two horizontal walls with the height of H ($0 < y < H$) (Fig. 1). For simplicity, the length of the computational domain L ($0 < x < L$) is chosen to equal H ($L = H$) unless otherwise stated. Initial sinusoidal perturbations are applied to the fluid–fluid interfaces. All

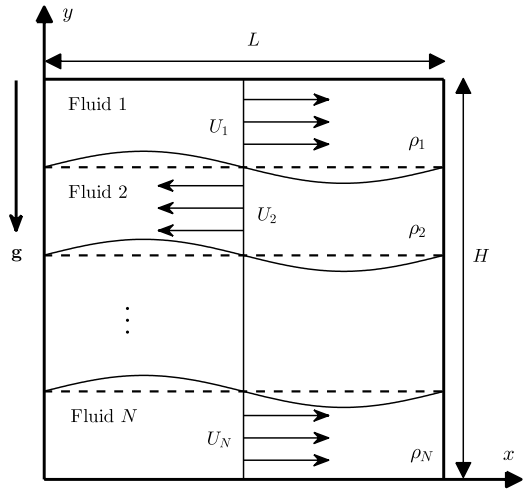

Fig. 1. Schematic illustration of the flow configuration.

quantities subscripted with a k are properties of the kth fluid for $k = 1, 2, \ldots, N$. For the densities of N fluids, it is always the case that $\rho_1 < \rho_2 < \cdots < \rho_N$ so that buoyancy effects do not dominate. Each fluid has a base horizontal speed U_k.

To non-dimensionalize the governing equations (4)–(7), we define characteristic quantities of length (L_c), velocity (U_c), density (ρ_c), viscosity (η_c), and chemical potential (μ_c). In our simulations, we choose $L_c = H$, $U_c = \max_k U_k$, $\rho_c = \rho_N$, and $\eta_c = \eta_N$. We then introduce the following dimensionless variables:

$$\mathbf{x}' = \frac{\mathbf{x}}{L_c}, \quad \mathbf{u}' = \frac{\mathbf{u}}{U_c}, \quad t' = \frac{t U_c}{L_c}, \quad \rho' = \frac{\rho}{\rho_c},$$
$$p' = \frac{p}{\rho_c U_c^2}, \quad \eta' = \frac{\eta}{\eta_c}, \quad \mathbf{g}' = \frac{\mathbf{g}}{g}, \quad \mu_k{}' = \frac{\mu_k}{\mu_c},$$

where the primed quantities are dimensionless. Substituting these variables into Eqs. (4)–(7) and dropping the primes, we have for $k = 1, 2, \ldots, N$,

$$\rho(\mathbf{c}) \left(\frac{\partial \mathbf{u}}{\partial t} + \mathbf{u} \cdot \nabla \mathbf{u} \right) = -\nabla p + \frac{1}{\mathrm{Re}} \nabla \cdot \left[\eta(\mathbf{c}) (\nabla \mathbf{u} + \nabla \mathbf{u}^{\mathrm{T}}) \right] + \mathbf{SF}(\mathbf{c}) + \frac{\rho(\mathbf{c})}{\mathrm{Fr}^2} \mathbf{g}, \tag{8}$$

$$\nabla \cdot \mathbf{u} = 0, \tag{9}$$

$$\frac{\partial c_k}{\partial t} + \nabla \cdot (c_k \mathbf{u}) = \frac{1}{\mathrm{Pe}} \Delta \mu_k, \tag{10}$$

$$\mu_k = f(c_k) - \epsilon^2 \Delta c_k + \beta_k, \tag{11}$$

where $\mathbf{SF}(\mathbf{c}) = \sum_{i=1}^{N-1} \left(\sum_{j=i+1}^{N} 0.5 [\mathbf{sf}(c_i) + \mathbf{sf}(c_j)] \delta(c_i, c_j) / \mathrm{We}_{ij} \right)$, $\mathbf{g} = (0, -1)$, and ϵ is redefined according to the scaling. The dimensionless parameters are the Reynolds number, $\mathrm{Re} = \rho_c U_c L_c / \eta_c$, the Weber number of fluids i and j, $\mathrm{We}_{ij} = \rho_c L_c U_c^2 / \sigma_{ij}$, the Froude number, $\mathrm{Fr} = U_c / \sqrt{g L_c}$, and the Péclet number, $\mathrm{Pe} = U_c L_c / (M \mu_c)$. The governing equations (8)–(11) are considered with the following boundary conditions: at the top and bottom of the domain Ω we apply $\frac{\partial u}{\partial y} = v = \frac{\partial p}{\partial y} = \frac{\partial c_k}{\partial y} = \frac{\partial \mu_k}{\partial y} = 0$, while at the sides of Ω we impose the periodic boundary conditions.

4. Numerical solution

Let a two-dimensional computational domain be uniformly partitioned with spacing h. The cell center is located at $(x_i, y_j) = ((i - 0.5)h, (j - 0.5)h)$ for $i = 1, \ldots, N_x$ and $j = 1, \ldots, N_y$. N_x and N_y are the numbers of cells in the x- and y-directions, respectively.

Cell vertices are located at $(x_{i+\frac{1}{2}}, y_{j+\frac{1}{2}}) = (ih, jh)$. Pressures and vector-valued phase-fields are stored at cell centers, and velocities are stored at cell faces [71]. Let Δt be the dimensionless time step and n be the time step index. At the beginning of each time step, given $\mathbf{u}^n$ and $\mathbf{c}^n$, we want to find $\mathbf{u}^{n+1}$, $\mathbf{c}^{n+1}$, and p^{n+1} that solve the following discrete equations: for $k = 1, 2, \ldots, N-1$,

$$\rho^n \frac{\mathbf{u}^{n+1} - \mathbf{u}^n}{\Delta t} = -\nabla_d p^{n+1} + \frac{1}{\mathrm{Re}} \nabla_d \cdot \left[\eta^n (\nabla_d \mathbf{u}^n + (\nabla_d \mathbf{u}^n)^{\mathrm{T}})\right] + \mathbf{SF}^n + \frac{\rho^n}{\mathrm{Fr}^2}\mathbf{g} - \rho^n (\mathbf{u} \cdot \nabla_d \mathbf{u})^n, \tag{12}$$

$$\nabla_d \cdot \mathbf{u}^{n+1} = 0, \tag{13}$$

$$\frac{{c_k}^{n+1} - {c_k}^n}{\Delta t} = \frac{1}{\mathrm{Pe}} \Delta_d {\mu_k}^{n+1} + \frac{1}{\mathrm{Pe}} \Delta_d \left({\beta_k}^n - \frac{1}{4}{c_k}^n\right) - \nabla_d \cdot (c_k \mathbf{u})^n, \tag{14}$$

$${\mu_k}^{n+1} = \varphi({c_k}^{n+1}) - \epsilon^2 \Delta_d {c_k}^{n+1}, \tag{15}$$

where $\rho^n = \rho(\mathbf{c}^n)$, $\eta^n = \eta(\mathbf{c}^n)$, $\mathbf{SF}^n = \mathbf{SF}(\mathbf{c}^n)$, and $\varphi(c_k) = f(c_k) + 0.25 c_k$ is a nonlinear function. Note that we need only solve these equations with $c_1, c_2, \ldots, c_{N-1}$, because $c_N = 1 - \sum_{k=1}^{N-1} c_k$. The main procedure for solving Eqs. (12)–(15) in each time step is as follows.

Step 1. Initialize $\mathbf{u}^0$ to be the divergence-free velocity field and ${c_k}^0$ for $k = 1, 2, \ldots, N-1$.

Step 2. An intermediate velocity field, $\tilde{\mathbf{u}}$, is calculated without the pressure gradient term:

$$\frac{\tilde{\mathbf{u}} - \mathbf{u}^n}{\Delta t} = \frac{1}{\rho^n \mathrm{Re}} \nabla_d \cdot \left[\eta^n (\nabla_d \mathbf{u}^n + (\nabla_d \mathbf{u}^n)^{\mathrm{T}})\right] + \frac{\mathbf{SF}^n}{\rho^n} + \frac{\mathbf{g}}{\mathrm{Fr}^2} - (\mathbf{u} \cdot \nabla_d \mathbf{u})^n,$$

where the convective term, $(\mathbf{u} \cdot \nabla_d \mathbf{u})^n$, is computed using an upwind scheme [72]. The following pressure Poisson equation is then solved by a linear multigrid method [73] to obtain the pressure needed to enforce incompressibility:

$$\nabla_d \cdot \left(\frac{1}{\rho^n} \nabla_d p^{n+1}\right) = \frac{1}{\Delta t} \nabla_d \cdot \tilde{\mathbf{u}}.$$

Then we obtain the divergence-free velocity field: $\mathbf{u}^{n+1} = \tilde{\mathbf{u}} - \frac{\Delta t}{\rho^n} \nabla_d p^{n+1}$.

Step 3. Update the phase-field ${c_k}^n$ to ${c_k}^{n+1}$ for $k = 1, 2, \ldots, N-1$. In order to solve the N-component CH system (14) and (15) in a decoupled way (this allows us to reduce the CPU time and memory requirements), we use the recently developed practically unconditionally stable scheme [44]. Note that, for mass conservation, we use a conservative discretization of the convective part of the phase-field equation (14):

$$\left[(c_k u)_x + (c_k v)_y\right]_{ij}^n = \frac{u^n_{i+\frac{1}{2},j}({c_k}^n_{i+1,j} + {c_k}^n_{ij}) - u^n_{i-\frac{1}{2},j}({c_k}^n_{ij} + {c_k}^n_{i-1,j})}{2h} + \frac{v^n_{i,j+\frac{1}{2}}({c_k}^n_{i,j+1} + {c_k}^n_{ij}) - v^n_{i,j-\frac{1}{2}}({c_k}^n_{ij} + {c_k}^n_{i,j-1})}{2h}.$$

This completes the single time-step process.

5. Numerical experiments

In this section, we describe a number of numerical experiments for two- and three-component fluids in two dimensions. In our numerical experiments, the fluid viscosities are matched and we define the function $l(x, y; a, b)$ as $l(x, y; a, b) := \tanh\left[(y - b - 0.01\sin(a\pi x))/(2\sqrt{2}\epsilon)\right]$ for simplicity of notation.

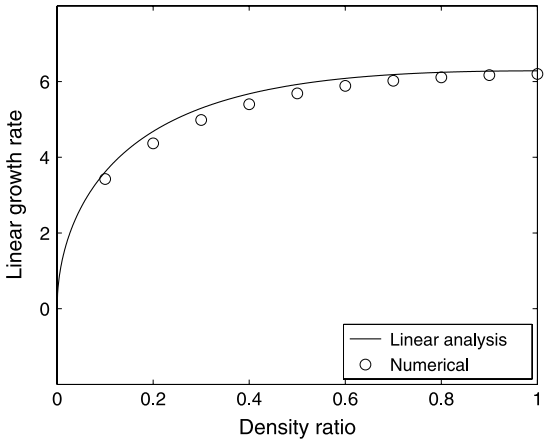

Fig. 2. Results of linear growth rate from analysis and simulation at different density ratio r.

5.1. Linear growth rate for the Kelvin–Helmholtz instability of two-component fluids

The two-fluid system can be perturbed by applying a sinusoidal disturbance on the fluid–fluid interface in the form of

$$A = A_0 e^{ikx+nt},$$

where k is the wave number. When both gravitational and surface tension forces are present, it is found that [74]

$$n = -ik\frac{\rho_1 U_1 + \rho_2 U_2}{\rho_1 + \rho_2} \pm \sqrt{\frac{k^2 \rho_1 \rho_2 (U_1 - U_2)^2}{(\rho_1 + \rho_2)^2} - \frac{kg(\rho_2 - \rho_1)}{\rho_1 + \rho_2} - \frac{k^3 \sigma}{\rho_1 + \rho_2}}.$$

The real and imaginary parts of n are the linear growth rate $\gamma = \mathrm{Re}(n)$ and frequency $\omega = -\mathrm{Im}(n)$, respectively.

In order to calculate the numerical growth rate at different density ratio $r = \rho_1/\rho_2$, we take the initial conditions as

$$c(x, y, 0) = 0.5\,(1 + l(x, y; 2, 0.5))\,,$$
$$u(x, y, 0) = l(x, y; 2, 0.5), \qquad v(x, y, 0) = 0$$

on the domain $\Omega = [0, 1] \times [0, 1]$. Here, we use $h = 1/256$, $\Delta t = 0.064h$, $\epsilon = 0.02$, $\mathrm{Pe} = 10/\epsilon$, and $\mathrm{Re} = 5000$. In this test, we let $g = \sigma = 0$. Therefore, the analytical non-dimensional growth rate γ_e can be written as

$$\gamma_e = \frac{4\pi\sqrt{r}}{1 + r}.$$

For numerical investigation, the numerical growth rate γ_n is calculated in the form of [28]

$$\gamma_n = \frac{A(t)/A_0 - 1}{t}.$$

In Fig. 2, we compare the results from analysis and simulation at different density ratio r. As shown in Fig. 2, the simulation results agree well with the analytical results.

5.2. Kelvin–Helmholtz instability of two-component fluids

We here consider the KH instability of two-component fluids. The initial conditions are

$$c(x, y, 0) = 0.5\,(1 + l(x, y; 2, 0.5))\,,$$
$$u(x, y, 0) = l(x, y; 2, 0.5), \qquad v(x, y, 0) = 0$$

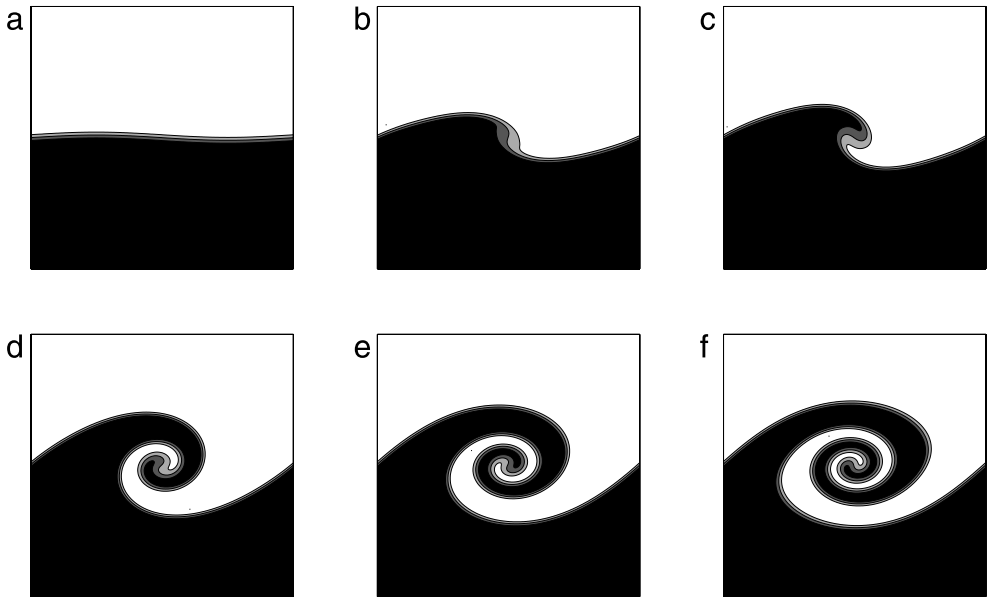

Fig. 3. Evolution of the phase-field with a single-mode sinusoidal interface perturbation at dimensionless times (a) $t = 0$, (b) $t = 0.6$, (c) $t = 0.7$, (d) $t = 1$, (e) $t = 1.2$, and (f) $t = 1.4$. In each figure, the levels of gray-scale-filled contours are from 0 to 0.25 (black), from 0.25 to 0.5 (dark gray), from 0.5 to 0.75 (gray), and from 0.75 to 1 (white).

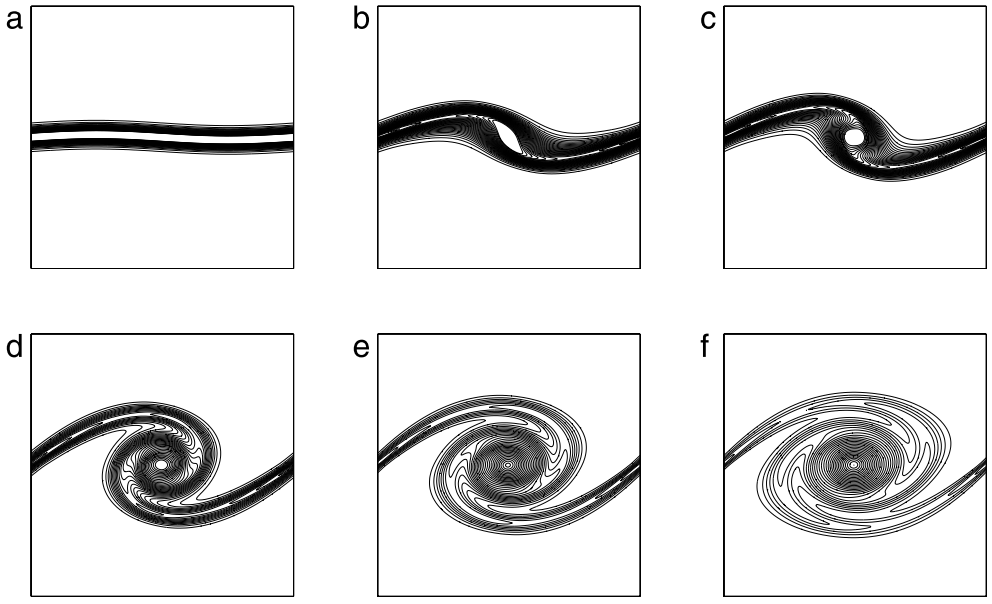

Fig. 4. Evolution of the vorticity field $(v_x - u_y)$ displayed as contours at dimensionless times (a) $t = 0$, (b) $t = 0.6$, (c) $t = 0.7$, (d) $t = 1$, (e) $t = 1.2$, and (f) $t = 1.4$. The highest contour level is 0.1. Succeeding levels are decreased by 1.

on the domain $\Omega = [0, 1] \times [0, 1]$. Here, we use $h = 1/256$, $\Delta t = 0.128h$, $\epsilon = 0.01/\sqrt{2}$, and $\mathrm{Pe} = 10/\epsilon$. The remaining parameter values are $\rho_1 : \rho_2 = 0.99 : 1$, $\mathrm{Re} = 5000$, and $\mathrm{Fr} = 1$. In this test, the surface tension is neglected. Fig. 3 shows the evolution of the phase-field with a single-mode sinusoidal interface perturbation; the levels of gray-scale-filled contours are from 0 to 0.25 (black), from 0.25 to 0.5 (dark gray), from 0.5 to 0.75 (gray), and from 0.75 to 1 (white).

Early in the dynamics, the flow sweeps the initial interfacial vorticity into the center (Fig. 4), and the heavier and lighter fluids move in the positive and negative vertical directions, respectively, as a result, both fluids penetrate each other. As vorticity accumulates at the center, the interface begins to steepen and the height of the instability gets larger. At late time, roll-up follows and the interface evolves into a spiral with a "cat's eye" shape. The dynamics of the rolling interface is consistent with those obtained in two-dimensional simulations using immersed boundary type methods [22,23] and a multiple-relaxation-time lattice Boltzmann method [32].

Next, we take the same initial conditions and parameter values used to create Fig. 3 except for ϵ to investigate the effect of ϵ on the interface evolution. Fig. 5(a)–(c) show snapshots of the phase-field at dimensionless time $t = 1$ for $\epsilon = 0.02/\sqrt{2}, 0.01/\sqrt{2}$, and $0.005/\sqrt{2}$, respectively. $\epsilon = 0.02/\sqrt{2}$ is relatively large (Pe is small), and the diffusion term in the phase-field equation is dominant (Fig. 5(a)). Ideally, we want to minimize the diffusion effect of the phase-field, because we are primarily interested in the hydrodynamics of the multiphase system. Next, let us consider the other case. $\epsilon = 0.005/\sqrt{2}$ is relatively small (Pe is large), and the advection term in the phase-field equation is dominant. This implies that the interface is locally out of equilibrium. In Fig. 5(c), it can clearly be observed that the interfacial transition region is

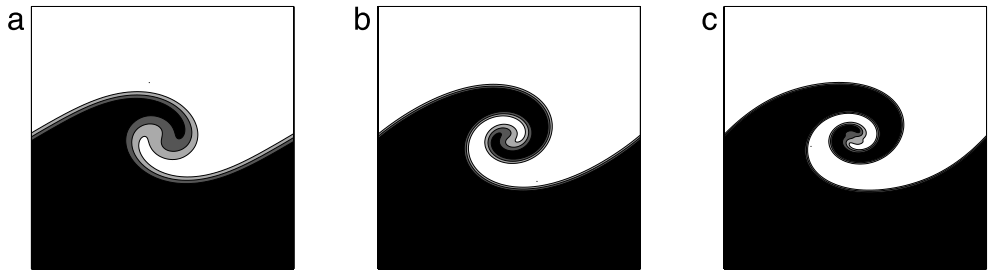

Fig. 5. Effect of ϵ on the interface evolution: snapshots of the phase-field at dimensionless time $t = 1$ for (a) $\epsilon = 0.02/\sqrt{2}$, (b) $\epsilon = 0.01/\sqrt{2}$, and (c) $\epsilon = 0.005/\sqrt{2}$. In each figure, the levels of gray-scale-filled contours are from 0 to 0.25 (black), from 0.25 to 0.5 (dark gray), from 0.5 to 0.75 (gray), and from 0.75 to 1 (white).

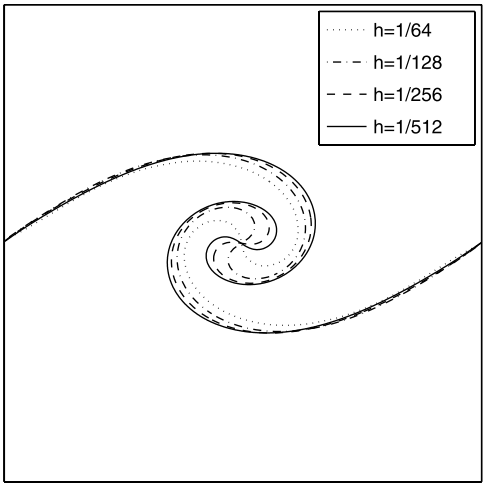

Fig. 6. Grid convergence study: interfaces obtained using 64×64 (dotted line), 128×128 (dashdot line), 256×256 (dashed line), and 512×512 (solid line) grid points at dimensionless time $t = 1$.

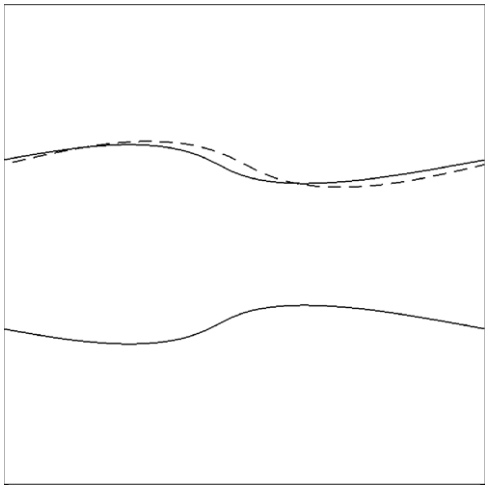

Fig. 7. Interfaces of two- (dashed line) and three- (solid lines) component fluids for density ratio = 1. For two-component fluids, the numerical growth rate is 6.2019. For three-component fluids, the numerical growth rates of upper and lower interfaces are 5.0610 and 4.8932, respectively.

not smooth. The interface evolution is sensitive to the value of ϵ. Decreasing the value of ϵ results in a non-smooth concentration profile, whereas increasing the value of ϵ results in too much diffusion. On the other hand, if an appropriate ϵ value ($\epsilon = 0.01/\sqrt{2}$) is taken, as in Fig. 5(b), we have both a smooth interfacial transition and rolling interface profile according to the flow field.

We finally perform a number of simulations for a sample initial problem on a set of increasingly finer grids. The numerical solutions are computed on the uniform grids $h = 1/2^n$ for $n = 6, 7, 8$, and 9. For each grid, $\Delta t = 2.5 \cdot 10^{-4}$, $\epsilon = 0.01$, $\rho_1 : \rho_2 = 0.99 : 1$, $\mathrm{Pe} = 1/\epsilon$, $\mathrm{Re} = 50\,000$, and $\mathrm{Fr} = 1$ are used. Fig. 6 shows the interfaces obtained using 64×64 (dotted line), 128×128 (dashdot line), 256×256 (dashed line), and 512×512 (solid line) grid points at dimensionless time $t = 1$. The convergence of the results under grid refinement is evident.

5.3. Comparison between the Kelvin–Helmholtz instability of two- and three-component fluids

In order to investigate the effect of inclusion of extra layers on the growth rate for the KH instability, we consider the three-component fluids with the following initial conditions:

$$c_1(x, y, 0) = 0.5\,(1 + l(x, y; 2, 2/3))\,,$$
$$c_2(x, y, 0) = 0.5\,(1 + l(x, y; -2, 1/3)) - c_1(x, y, 0),$$
$$u(x, y, 0) = 1 + l(x, y; 2, 2/3) - l(x, y; -2, 1/3),$$
$$v(x, y, 0) = 0$$

on the domain $\Omega = [0, 1] \times [0, 1]$. Here, we use $h = 1/256$, $\Delta t = 0.064h$, $\epsilon = 0.02$, $\mathrm{Pe} = 10/\epsilon$, $\mathrm{Re} = 5000$, and $\rho_1 : \rho_2 : \rho_3 = 1 : 1 : 1$. In this test, the gravity and surface tension are neglected.

Fig. 7 shows the interfaces of two- and three-component fluids. Dashed line represents the interface (shifted up to overlap) in Section 5.1 when the density ratio is equal to 1. Solid lines represent the interfaces of three-component fluids. In Section 5.1, we observed that the numerical growth rate is 6.2019 when the density ratio is equal to 1. However, in the case of three-component fluids, the upper and lower interfaces are influenced by each other. Thus, the numerical growth rates of upper and lower interfaces are 5.0610 and 4.8932, respectively. From this result, we see that the inclusion of extra layers can alter the growth rate for the KH instability.

5.4. Kelvin–Helmholtz instability of three-component fluids

In the rest of this paper, we will deal mainly with three-component fluids (in Section 5.11, we will also deal with four- and five-component fluids). For two-component fluids, we plot gray-scale-filled contours with several levels to show some mixing between the fluids (see Figs. 3 and 5). However, for three-component fluids, we plot filled contours at only one level for each fluid to clearly recognize the interface evolution of three-component fluids. In Figs. 8 and 10–15, the fluids 1, 2, and 3 are represented by gray, white, and black colors, respectively. The color contrast of each fluid is obtained by shifting the value of the phase-field variable by adding a constant and by taking the contour of each different level. The following MATLAB code was used to create the figure: `colormap gray;contourf(C1+1,[1.5 1.5]); hold on;contourf(C2+2,[2.5 2.5]);contourf(C3, [0.5 0.5]);`.

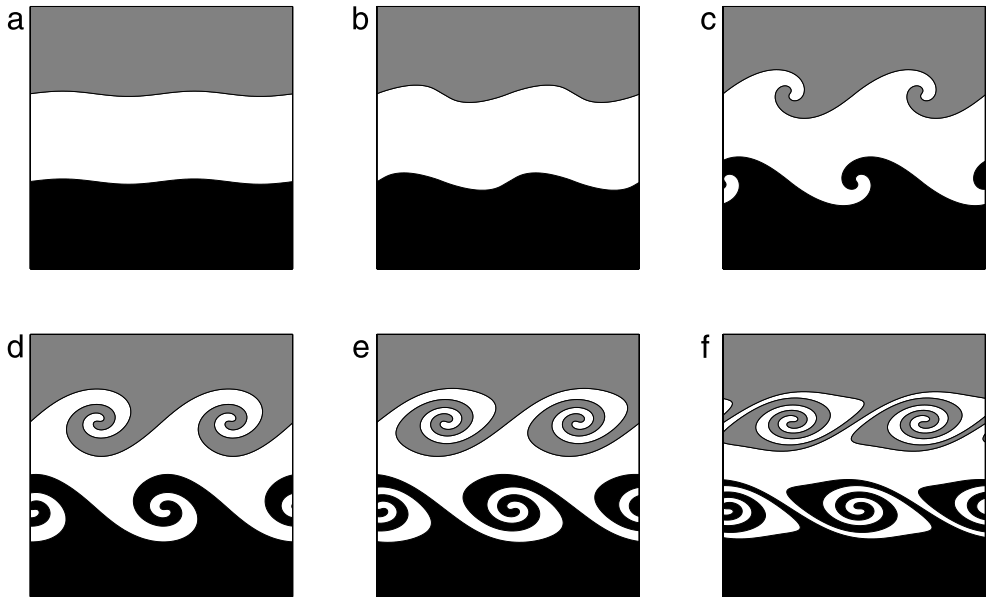

Fig. 8. Evolution of the phase-field with two-mode sinusoidal interface perturbations at dimensionless times (a) $t = 0$, (b) $t = 0.2$, (c) $t = 0.4$, (d) $t = 0.6$, (e) $t = 0.8$, and (f) $t = 1$.

In order to model the KH instability of three-component fluids, we take the initial conditions as

$$c_1(x, y, 0) = 0.5\,(1 + l(x, y; 4, 2/3))\,, \tag{16}$$

$$c_2(x, y, 0) = 0.5\,(1 + l(x, y; 4, 1/3)) - c_1(x, y, 0), \tag{17}$$

$$u(x, y, 0) = 1 + l(x, y; 4, 2/3) - l(x, y; 4, 1/3), \tag{18}$$

$$v(x, y, 0) = 0 \tag{19}$$

on the domain $\Omega = [0, 1] \times [0, 1]$. Here, we use $h = 1/256$, $\Delta t = 0.128h$, $\epsilon = 0.006/\sqrt{2}$, and $\mathrm{Pe} = 10/\epsilon$. The remaining parameter values are $\rho_1 : \rho_2 : \rho_3 = 0.98 : 0.99 : 1$, $\mathrm{Re} = 5000$, and $\mathrm{Fr} = 1$. In this test, the surface tension is neglected. Fig. 8 shows the evolution of the phase-field with two-mode sinusoidal interface perturbations.

At each interface (fluid 1–fluid 2 and fluid 2–fluid 3), vorticity accumulates in the billow cores by advecting away from the braid centers (the braid refers to a thin tilted interface formed in the region between billow cores, see Fig. 9). This accumulation of vorticity results in the formation of thin braids and cores of vorticity. At $t = 0.8$, the billows are close to their saturation state, where the braids are thinnest and the cores have maximum strength. After passing the saturation state, the billow height and core vorticity concentration relax back. Note that, due to the difference in the direction of the horizontal velocity of the upper (or lower) layer of each interface, the cores of vorticity at the interface between fluids 2 and 3 are more moved to the left than those at the interface between fluids 1 and 2.

5.5. Effect of Weber number

In order to examine the effect of surface tension on the interface evolution, we take the same initial conditions (Eqs. (16)–(19)) and parameter values used to create Fig. 8 except for the Weber number. Fig. 10(a)–(c) show snapshots of the phase-field at dimensionless time $t = 0.8$ for $\mathrm{We}_{ij} = 1000$, 100, and 10, respectively. At a sufficiently large Weber number $\mathrm{We}_{ij} = 1000$, the elongated interface rolls up by following the evolution of the flow. At $\mathrm{We}_{ij} = 100$, surface tension retards roll-up of the elongated interface and the interfacial ends are blunt due to the smoothing effect of surface tension. When surface tension becomes much stronger $\mathrm{We}_{ij} = 10$, the interface roll-up is completely suppressed.

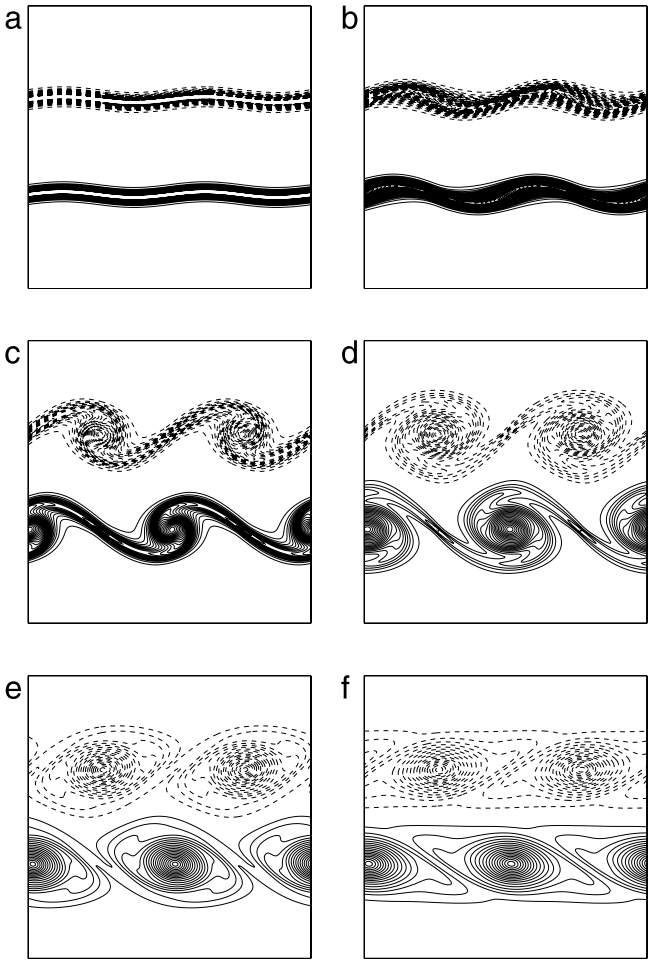

Fig. 9. Evolution of the vorticity field ($v_x - u_y$) displayed as contours at dimensionless times (a) $t = 0$, (b) $t = 0.2$, (c) $t = 0.4$, (d) $t = 0.6$, (e) $t = 0.8$, and (f) $t = 1$. Solid lines represent positive vorticity. The lowest contour level is 1 and succeeding levels are increased by 2. Dashed lines represent negative vorticity. The highest contour level is -1 and succeeding levels are decreased by 2.

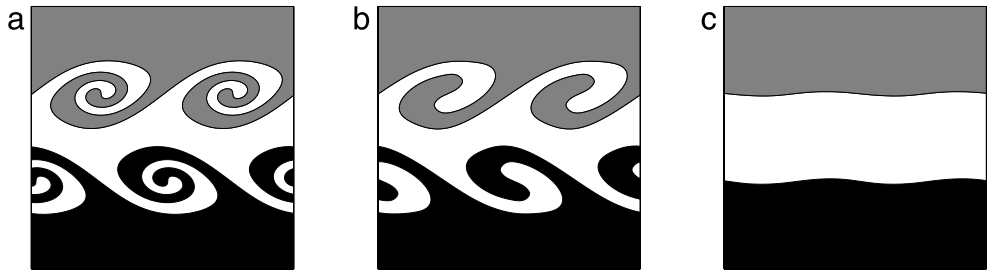

Fig. 10. Effect of Weber number on the interface evolution: snapshots of the phase-field at dimensionless time $t = 0.8$ for (a) $We_{ij} = 1000$, (b) $We_{ij} = 100$, and (c) $We_{ij} = 10$.

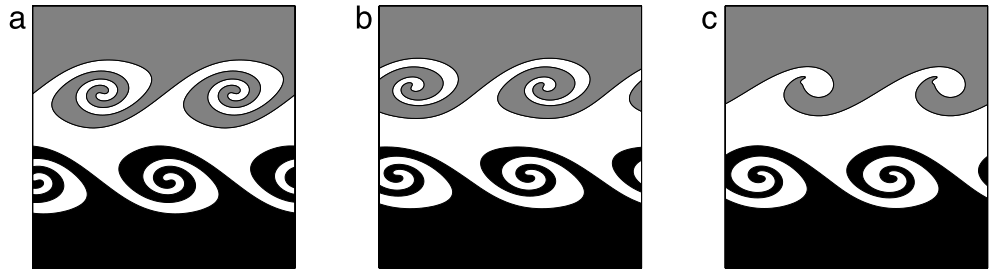

Fig. 11. Effect of density ratio on the interface evolution: snapshots of the phase-field at dimensionless time $t = 0.8$ for (a) $\rho_1 : \rho_2 : \rho_3 = 0.98 : 0.99 : 1$, (b) $\rho_1 : \rho_2 : \rho_3 = 0.4 : 0.7 : 1$, and (c) $\rho_1 : \rho_2 : \rho_3 = 0.1 : 0.55 : 1$.

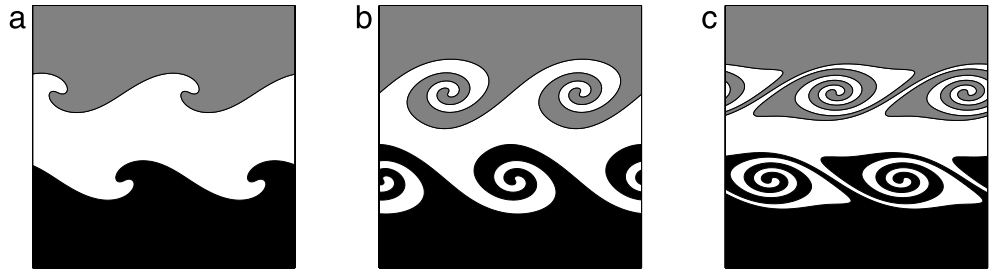

Fig. 12. Effect of magnitude of velocity difference on the interface evolution: snapshots of the phase-field at dimensionless time $t = 0.7$ for the initial horizontal velocities in (a) Eq. (20), (b) Eq. (18), and (c) Eq. (21).

5.6. Effect of density ratio

In order to investigate the effect of density ratio on the interface evolution, we take the same initial conditions (Eqs. (16)–(19)) and parameter values used to create Fig. 8 except for the density ratio. Fig. 11(a)–(c) show snapshots of the phase-field at dimensionless time $t = 0.8$ for $\rho_1 : \rho_2 : \rho_3 = 0.98 : 0.99 : 1$, $0.4 : 0.7 : 1$, and $0.1 : 0.55 : 1$, respectively. As the density ratio increases, the stabilizing effect of stratification due to gravity becomes more pronounced, i.e., the KH instability becomes more suppressed. Note that with increasing density ratio, the transition from linear to non-linear stage is delayed to later simulation times.

5.7. Effect of magnitude of velocity difference

In order to study the effect of magnitude of velocity difference on the interface evolution, we take the initial condition same as in Eqs. (16) and (17) for the phase-field and in Eq. (19) for the vertical velocity component. For the horizontal velocity component, we take the initial condition in Eq. (18) and the following two initial conditions:

$$u(x, y, 0) = 1 + 0.505[l(x, y; 4, 2/3) - l(x, y; 4, 1/3)], \tag{20}$$

and

$$u(x, y, 0) = 1 + 1.5[l(x, y; 4, 2/3) - l(x, y; 4, 1/3)], \tag{21}$$

on the domain $\Omega = [0, 1] \times [0, 1]$. The differences in initial horizontal velocities of fluids 1 and 2 (or fluids 2 and 3) are 1.01, 2, and 3 for Eqs. (20), (18), and (21), respectively. In this test, we take the same parameter values used to create Fig. 8. Fig. 12(a)–(c) show snapshots of the phase-field at dimensionless time $t = 0.7$ for the initial horizontal velocities in Eqs. (20), (18), and (21), respectively. As we can see in Fig. 12, the interface rolls up more as the initial horizontal velocity difference gets larger.

5.8. Effect of forcing

In order to examine the effect of forcing on the interface evolution, for the phase-field we take the initial condition in Eqs. (16) and (17) and the following two initial conditions:

$$c_1(x, y, 0) = 0.5\left[1 + \tanh\left(\frac{y - 2/3 - 0.02\sin(4\pi x)}{2\sqrt{2}\epsilon}\right)\right] \tag{22}$$

$$c_2(x, y, 0) = 0.5\left[1 + \tanh\left(\frac{y - 1/3 - 0.02\sin(4\pi x)}{2\sqrt{2}\epsilon}\right)\right] - c_1(x, y, 0) \tag{23}$$

and

$$c_1(x, y, 0) = 0.5\left[1 + \tanh\left(\frac{y - 2/3 - 0.05\sin(4\pi x)}{2\sqrt{2}\epsilon}\right)\right] \tag{24}$$

$$c_2(x, y, 0) = 0.5\left[1 + \tanh\left(\frac{y - 1/3 - 0.05\sin(4\pi x)}{2\sqrt{2}\epsilon}\right)\right] - c_1(x, y, 0) \tag{25}$$

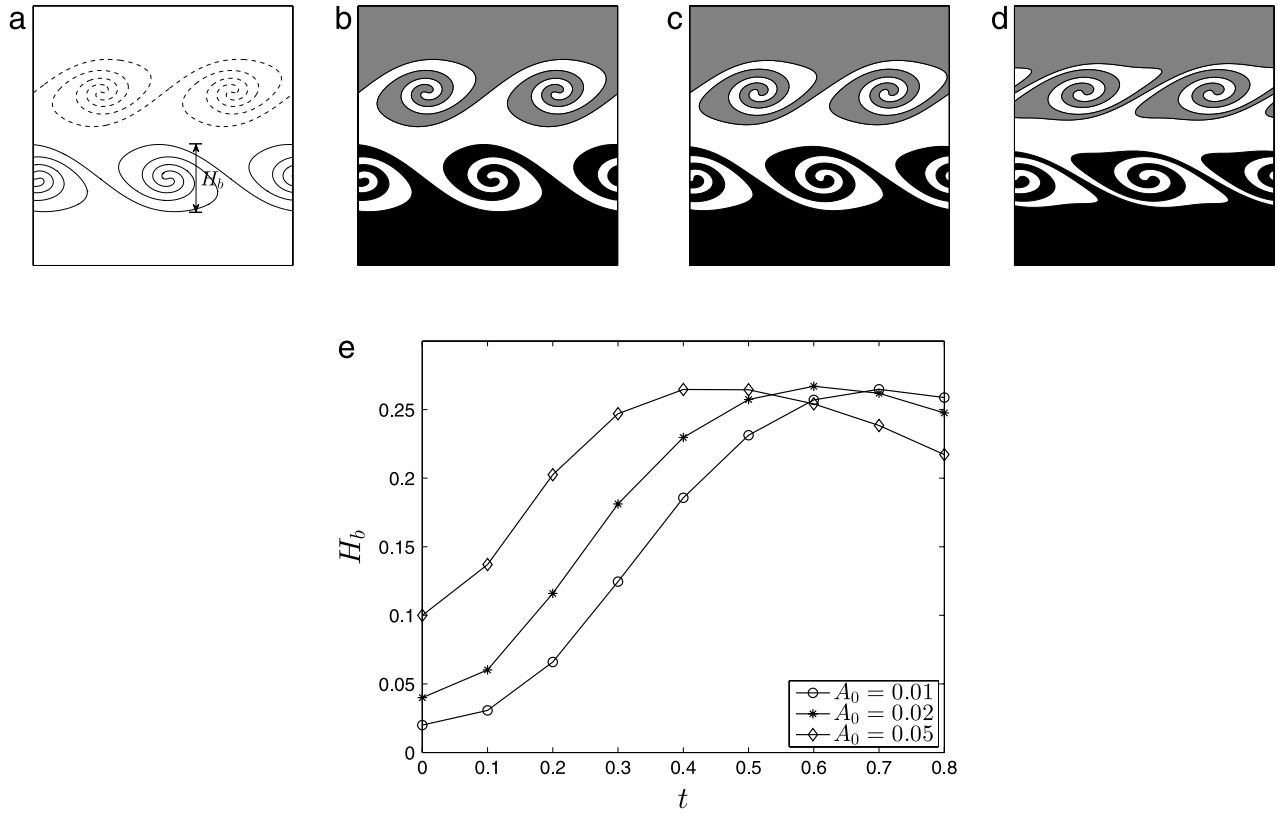

Fig. 13. Effect of forcing on the interface evolution. (a) Schematic representation of the billow height H_b. (b)–(d) Snapshots of the phase-field at dimensionless time $t = 0.8$ for $A_0 = 0.01$, 0.02, and 0.05. (e) Time evolution of the billow height for each A_0.

on the domain $\Omega = [0, 1] \times [0, 1]$. The initial wave amplitudes, A_0, are 0.01, 0.02, and 0.05 for Eqs. (16) and (17), (22) and (23), and (24) and (25), respectively. In this test, we take the same parameter values used to create Fig. 8. Note that the height of the billow, H_b, is defined as the vertical distance between the highest and lowest points of the braid (see Fig. 13(a)). Fig. 13(b)–(d) show snapshots of the phase-field at dimensionless time $t = 0.8$ for $A_0 = 0.01$, 0.02, and 0.05, respectively. For each A_0, the time evolution of the billow height is shown in Fig. 13(e). As we can see in Fig. 13, the billow height reaches its maximum more slowly as the initial wave amplitude gets smaller.

5.9. Effect of non-monotonic density variation

We here investigate a case where the density variation is non-monotonic. The initial condition for the phase-field is same as in Eqs. (16) and (17), and the same parameter values used to create Fig. 8 except for the density ratio are chosen. We take the density ratio as $\rho_1 : \rho_2 : \rho_3 = 1/2 : 1/6 : 1$ and the initial velocity as $u(x, y, 0) = 0.7 + 0.25l(x, y; 4, 2/3) - 0.55l(x, y; 4, 1/3)$, $v(x, y, 0) = 0$ to see the effect of non-monotonic density variation more clearly. Fig. 14 shows the evolution of the phase-field with non-monotonic density variation. Due to the given density variation, both Rayleigh–Taylor and KH instabilities are developed at the interface between fluids 1 and 2, whereas at the interface between fluids 2 and 3, the KH instability is suppressed. As a result, one interface becomes stabilized and the other one becomes destabilized as time goes by.

5.10. Simulation of the billowing cloud formation

The KH instability of multi-component fluids can be observed in a wide variety of natural situations. A classic example is the spectacular billowing cloud formation in the lower atmosphere (see Fig. 15(a)). In order to simulate this natural phenomenon, we take the initial conditions as

$$
\begin{aligned}
c_1(x, y, 0) &= 0.5\,(1 + l(x, y; 2, 4/7))\,,\\
c_2(x, y, 0) &= 0.5\,(1 + l(x, y; 2, 2.5/7)) - c_1(x, y, 0),\\
u(x, y, 0) &= -0.5\tanh\left[(y - 4/7 - \delta(x))/(2\sqrt{2}\epsilon)\right]\\
&\quad - 0.25\tanh\left[(y - 3/7 - \delta(x))/(2\sqrt{2}\epsilon)\right],\\
v(x, y, 0) &= 0
\end{aligned}
$$

on the domain $\Omega = [0, 7] \times [0, 1]$. The function $\delta(x)$ is defined as $\delta(x) = \sum_{i=1}^{6}[H(x-p_i) - H(x-p_{i+1})]q_i \sin[2\pi\,(x-p_i)/(p_{i+1}-p_i)]$, where $H(x)$ is the heaviside function and $p_1 = 0$, $p_2 = 1.16$, $p_3 = 2.43$, $p_4 = 3.55$, $p_5 = 4.71$, $p_6 = 5.78$, $p_7 = 7$, $q_1 = 0.011$, $q_2 = 0.012$, $q_3 = 0.009$, $q_4 = 0.011$, $q_5 = 0.01$, $q_6 = 0.008$. These values are chosen by trial and error to achieve a resemblance to the photograph in Fig. 15(a). Here, we use $h = 1/64$, $\Delta t = 0.128h$, $\epsilon = 0.006\sqrt{2}$, and $\mathrm{Pe} = 1/\epsilon$. The remaining parameter values are $\rho_1 : \rho_2 : \rho_3 = 0.98 : 0.99 : 1$, $\mathrm{Re} = 50\,000$, $\mathrm{Fr} = 0.1$, and $\mathrm{We}_{12} = \mathrm{We}_{13} = \mathrm{We}_{23} = 1000$. Fig. 15(b)–(e) show the evolution of the phase-field.

When two-component fluids are considered to simulate the billowing cloud formation, i.e., we consider, in Fig. 15(b), that the top and bottom layers consist of one fluid and the middle layer is another fluid, then gravity effect becomes dominant since the heavier fluid is superposed over the lighter fluid. However, with three-component fluids of different densities which are gradually increased toward the gravitational direction, we can simulate the billowing cloud formation as we can see in Fig. 15(b)–(e). In this simulation, the details of the real flow (e.g., the asymmetry in the roll-up and the self-interaction of the shear layer) are well captured.

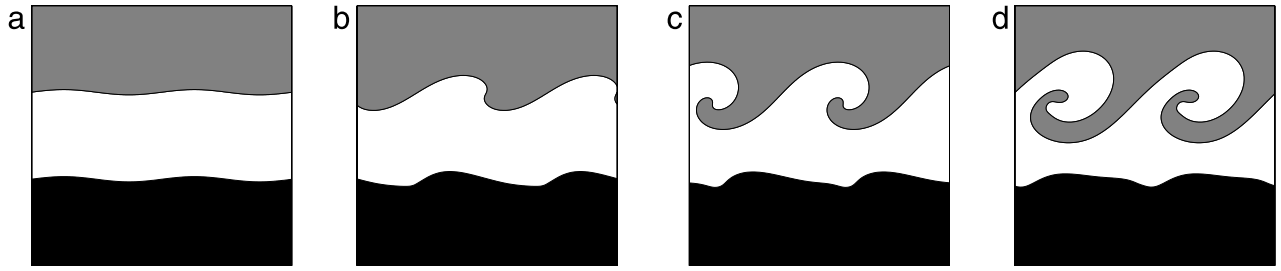

Fig. 14. Evolution of the phase-field with non-monotonic density variation at dimensionless times (a) $t = 0$, (b) $t = 1$, (c) $t = 1.5$, and (d) $t = 2$.

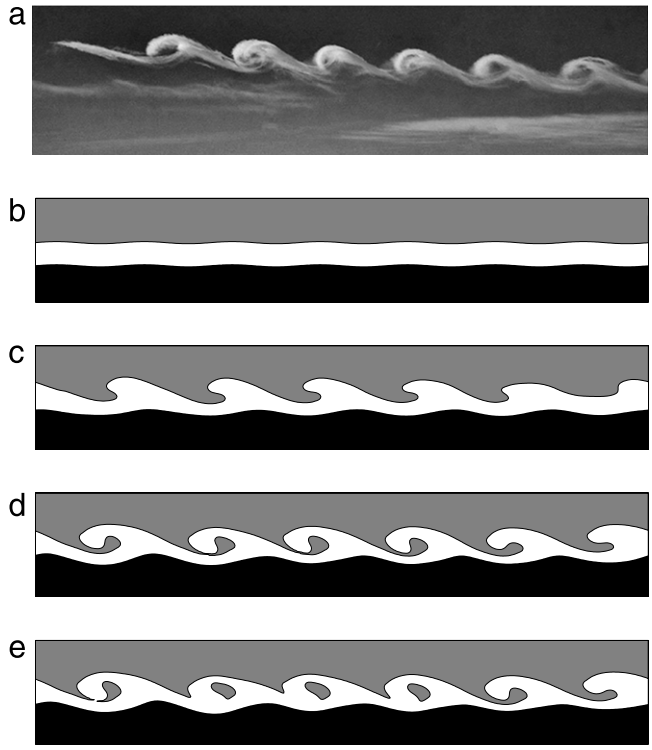

Fig. 15. Simulation of the billowing cloud formation: (a) photograph of KH billows in the atmosphere (this is available at: http://www.pinterest.com/timbrice/kelvin\T1\ndashhelmholtz-clouds/) and (b)–(e) numerical results of the KH instability of three-component fluids with density contrast at dimensionless times (b) $t = 0$, (c) $t = 2.1$, (d) $t = 3.3$, and (e) $t = 3.6$.

5.11. Efficiency of the numerical algorithm

With the numerical algorithm, we can solve the N-component CH system in a decoupled way, i.e., we only solve the binary CH equation $N - 1$ times to solve the system. In order to show the efficiency of the numerical algorithm, we consider the KH instability in N-layer flow. For $N = 2, 3, 4, 5$, the initial conditions

Table 1
CPU time (s) for N-layer flow during 1600 time steps.

N	2	3	4	5
CPU time	1206.749	2611.610	3895.531	5134.110

are

$$c_1(x, y, 0) = 0.5\,(1 + l(x, y; 2, (N-1)/N))\,,$$
$$c_k(x, y, 0) = 0.5(l(x, y; 2, (N-k)/N) - l(x, y; 2, (N-k+1)/N)) \quad \text{for } k = 1, 2, \ldots, N-1,$$
$$u(x, y, 0) = \mathrm{mod}(N, 2) + \sum_{k=1}^{N-1}(-1)^{k+1} l(x, y; 2, (N-k)/N),$$
$$v(x, y, 0) = 0$$

on the domain $\Omega = [0, 1] \times [0, 1]$. Here, we use $h = 1/256$, $\Delta t = 0.128h$, $\epsilon = 0.006/\sqrt{2}$, and $\mathrm{Pe} = 10/\epsilon$. The remaining parameter values are $\rho_1 : \rho_2 : \cdots : \rho_N = (1 - 0.01(N-1)) : (1 - 0.01(N-2)) : \cdots : 1$, $\mathrm{Re} = 5000$, and $\mathrm{Fr} = 1$. In this test, the surface tension is neglected. Simulations are performed on a 3.2 GHz Intel Core i5 CPU with 4 GB of RAM. Table 1 provides the CPU time (in seconds) during 1600 time steps for each number of layers. It can be seen that the CPU time increases almost linearly with the number of layers. Fig. 16 shows snapshots of the phase-field at dimensionless time $t = 0.8$ for N-layer flow.

6. Conclusions

The KH instability of multi-component (more than two) incompressible and immiscible fluids was studied numerically using a phase-field model. The instability was governed by the modified Navier–Stokes equations and the multi-component convective CH equations. A finite difference method was used to discretize the governing system. To solve the equations efficiently and accurately, we employed the Chorin's projection method for the modified Navier–Stokes equations and the recently developed practically unconditionally stable method for the multi-component CH equations. The algorithm was validated by simulating the KH instability of two-component fluids. The results

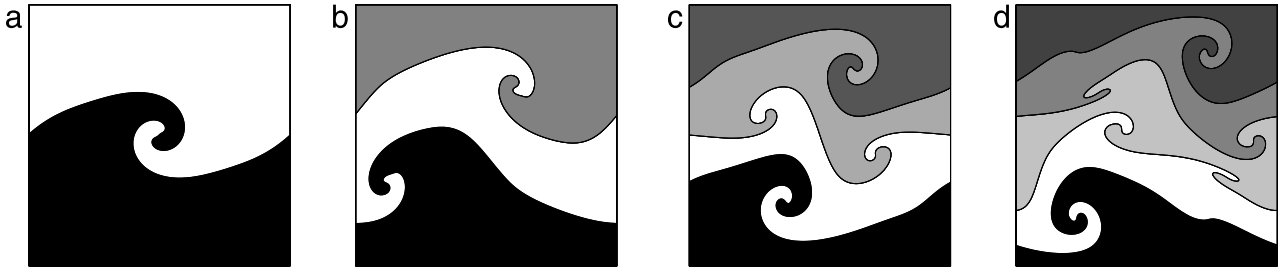

Fig. 16. Snapshots of the phase-field at dimensionless time $t = 0.8$ for (a) 2-, (b) 3-, (c) 4-, and (d) 5-layer flows.

of the present study for two-component fluids were consistent with previous results. Using the validated code, we investigated the effects of surface tension, density ratio, magnitude of velocity difference, and forcing on the KH instability of three-component fluids. It was shown that increasing the surface tension or the density ratio reduces the growth of the KH instability. Note that the surface tension may destabilize the short-waves. But, in our view, investigating that numerically is a nontrivial work. Therefore, we will consider this issue in future work. And it was also observed that as the initial horizontal velocity difference gets larger, the interface rolls up more. We also found that the billow height reaches its maximum more slowly as the initial wave amplitude gets smaller. And, for the linear growth rate for the KH instability of two-component fluids, the simulation results agreed well with the analytical results. From comparison between the numerical growth rate of two- and three-component fluids, we observed that the inclusion of extra layers can alter the growth rate for the KH instability. Finally, we simulated the billowing cloud formation for one set of parameters. With our multi-component method, the asymmetry in the roll-up and the self-interaction of the shear layer were well captured.

Acknowledgments

The first author (H.G. Lee) was supported by Basic Science Research Program through the National Research Foundation of Korea (NRF) funded by the Ministry of Education (2009-0093827). The authors thank the reviewers for the constructive and helpful comments on the revision of this article.

References

[1] W.D. Smyth, Kelvin–Helmholtz billow evolution from a localized source, Q. J. R. Meteorol. Soc. 130 (2004) 2753–2766.
[2] A. Mastrano, A. Melatos, Kelvin–Helmholtz instability and circulation transfer at an isotropic–anisotropic superfluid interface in a neutron star, Mon. Not. R. Astron. Soc. 361 (2005) 927–941.
[3] L. Kelvin, Hydrokinetic solutions and observations, Phil. Mag. 42 (1871) 362–377.
[4] H. Helmholtz, On discontinuous movements of fluids, Phil. Mag. 36 (1868) 337–346.
[5] G.I. Taylor, Effect of variation in density on the stability of superposed streams of fluid, Proc. R. Soc. A 132 (1931) 499–523.
[6] J.W. Miles, On the stability of heterogeneous shear flows. Part 2, J. Fluid Mech. 16 (1963) 209–227.
[7] P. Hazel, Numerical studies of the stability of inviscid stratified shear flows, J. Fluid Mech. 51 (1972) 39–61.
[8] S.A. Thorpe, A method of producing a shear flow in a stratified fluid, J. Fluid Mech. 32 (1968) 693–704.
[9] S.A. Thorpe, Turbulence in stably stratified fluids: a review of laboratory experiments, Bound.-Layer Meteorol. 5 (1973) 95–119.
[10] R.H. Rangel, W.A. Sirignano, Nonlinear growth of Kelvin–Helmholtz instability: effect of surface tension and density ratio, Phys. Fluids 31 (1988) 1845–1855.
[11] G.P. Klaassen, W.R. Peltier, The influence of stratification on secondary instability in free shear layers, J. Fluid Mech. 227 (1991) 71–106.
[12] M.M. Rogers, R.D. Moser, The three-dimensional evolution of a plane mixing layer: the Kelvin–Helmholtz rollup, J. Fluid Mech. 243 (1992) 183–226.
[13] C.P. Caulfield, W.R. Peltier, Three dimensionalization of the stratified mixing layer, Phys. Fluids 6 (1994) 3803–3805.
[14] A.B. Cortesi, G. Yadigaroglu, S. Banerjee, Numerical investigation of the formation of three-dimensional structures in stably-stratified mixing layers, Phys. Fluids 10 (1998) 1449–1473.
[15] W.D. Smyth, Dissipation-range geometry and scalar spectra in sheared stratified turbulence, J. Fluid Mech. 401 (1999) 209–242.
[16] C.P. Caulfield, W.R. Peltier, The anatomy of the mixing transition in homogeneous and stratified free shear layers, J. Fluid Mech. 413 (2000) 1–47.
[17] C. Staquet, Mixing in a stably stratified shear layer: two- and three-dimensional numerical experiments, Fluid Dynam. Res. 27 (2000) 367–404.
[18] R. Zhang, X. He, G. Doolen, S. Chen, Surface tension effects on two-dimensional two-phase Kelvin–Helmholtz instabilities, Adv. Water Resour. 24 (2001) 461–478.
[19] W.D. Smyth, J.N. Moum, D.R. Caldwell, The efficiency of mixing in turbulent patches: inferences from direct simulations and microstructure observations, J. Phys. Oceanogr. 31 (2001) 1969–1992.
[20] W. Tauber, S.O. Unverdi, G. Tryggvason, The nonlinear behavior of a sheared immiscible fluid interface, Phys. Fluids 14 (2002) 2871–2885.
[21] W.R. Peltier, C.P. Caulfield, Mixing efficiency in stratified shear flows, Annu. Rev. Fluid Mech. 35 (2003) 135–167.
[22] H.D. Ceniceros, A.M. Roma, Study of the long-time dynamics of a viscous vortex sheet with a fully adaptive nonstiff method, Phys. Fluids 16 (2004) 4285–4318.
[23] T.Y. Hou, Z. Shi, An efficient semi-implicit immersed boundary method for the Navier–Stokes equations, J. Comput. Phys. 227 (2008) 8968–8991.
[24] K.C. Sahu, H. Ding, P. Valluri, O.K. Matar, Linear stability analysis and numerical simulation of miscible two-layer channel flow, Phys. Fluids 21 (2009) 042104.
[25] K.C. Sahu, H. Ding, P. Valluri, O.K. Matar, Pressure-driven miscible two-fluid channel flow with density gradients, Phys. Fluids 21 (2009) 043603.
[26] A. Alexakis, Stratified shear flow instabilities at large Richardson numbers, Phys. Fluids 21 (2009) 054108.
[27] S.-I. Sohn, D. Yoon, W. Hwang, Long-time simulations of the Kelvin–Helmholtz instability using an adaptive vortex method, Phys. Rev. E 82 (2010) 046711.
[28] M.S. Shadloo, M. Yildiz, Numerical modeling of Kelvin–Helmholtz instability using smoothed particle hydrodynamics, Internat. J. Numer. Methods Engrg. 87 (2011) 988–1006.
[29] M.J. Chen, L.K. Forbes, Accurate methods for computing inviscid and viscous Kelvin–Helmholtz instability, J. Comput. Phys. 230 (2011) 1499–1515.
[30] P.R. Redapangu, K.C. Sahu, S.P. Vanka, A study of pressure-driven displacement flow of two immiscible liquids using a multiphase lattice Boltzmann approach, Phys. Fluids 24 (2012) 102110.
[31] P.R. Redapangu, K.C. Sahu, S.P. Vanka, A lattice Boltzmann simulation of three-dimensional displacement flow of two immiscible liquids in a square duct, J. Fluids Eng. 135 (2013) 121202.
[32] A. Fakhari, T. Lee, Multiple-relaxation-time lattice Boltzmann method for immiscible fluids at high Reynolds numbers, Phys. Rev. E 87 (2013) 023304.
[33] P.R. Redapangu, S.P. Vanka, K.C. Sahu, Multiphase lattice Boltzmann simulations of buoyancy-induced flow of two immiscible fluids with different viscosities, Eur. J. Mech. B Fluids 34 (2012) 105–114.
[34] L. Talon, N. Goyal, E. Meiburg, Variable density and viscosity, miscible displacements in horizontal Hele–Shaw cells. Part 1. Linear stability analysis, J. Fluid Mech. 721 (2013) 268–294.
[35] M.O. John, R.M. Oliveira, F.H.C. Heussler, E. Meiburg, Variable density and viscosity, miscible displacements in horizontal Hele–Shaw cells. Part 2. Nonlinear simulations, J. Fluid Mech. 721 (2013) 295–323.
[36] A. Ghasemi, B. Firoozabadi, M. Mahdinia, 2D numerical simulation of density currents using the SPH projection method, Eur. J. Mech. B Fluids 38 (2013) 38–46.
[37] R. Govindarajan, K.C. Sahu, Instabilities in viscosity-stratified flow, Annu. Rev. Fluid Mech. 46 (2014) 331–353.
[38] V.E. Badalassi, H.D. Ceniceros, S. Banerjee, Computation of multiphase systems with phase field models, J. Comput. Phys. 190 (2003) 371–397.
[39] J. Lowengrub, L. Truskinovsky, Quasi-incompressible Cahn–Hilliard fluids and topological transitions, Proc. R. Soc. Lond. Ser. A 454 (1998) 2617–2654.
[40] A.S. Utada, E. Lorenceau, D.R. Link, P.D. Kaplan, H.A. Stone, D.A. Weitz, Monodisperse double emulsions generated from a microcapillary device, Science 308 (2005) 537–541.
[41] J.M. Park, P.D. Anderson, A ternary model for double-emulsion formation in a capillary microfluidic device, Lab Chip 12 (2012) 2672–2677.
[42] C. Pozrikidis, Fluid Dynamics: Theory, Computation, and Numerical Simulation, Kluwer Academic Publishers, Boston, 2001.
[43] J. Kim, A generalized continuous surface tension force formulation for phase-field models for multi-component immiscible fluid flows, Comput. Methods Appl. Mech. Engrg. 198 (2009) 3105–3112.
[44] H.G. Lee, J.-W. Choi, J. Kim, A practically unconditionally gradient stable scheme for the N-component Cahn–Hilliard system, Physica A 391 (2012) 1009–1019.
[45] A.J. Chorin, A numerical method for solving incompressible viscous flow problems, J. Comput. Phys. 2 (1967) 12–26.
[46] H. Garcke, B. Nestler, B. Stoth, On anisotropic order parameter models for multi-phase systems and their sharp interface limits, Physica D 115 (1998) 87–108.
[47] B. Nestler, A.A. Wheeler, A multi-phase-field model of eutectic and peritectic alloys: numerical simulation of growth structures, Physica D 138 (2000) 114–133.
[48] B. Nestler, A.A. Wheeler, L. Ratke, C. Stöcker, Phase-field model for solidification of a monotectic alloy with convection, Physica D 141 (2000) 133–154.
[49] J.R. Green, A comparison of multiphase models and techniques, (Ph.D. thesis), The University of Leeds, Leeds, 2007.
[50] L. Vanherpe, F. Wendler, B. Nestler, S. Vandewalle, A multigrid solver for phase field simulation of microstructure evolution, Math. Comput. Simul. 80 (2010) 1438–1448.
[51] J.W. Cahn, J.E. Hilliard, Free energy of a nonuniform system. I. Interfacial free energy, J. Chem. Phys. 28 (1958) 258–267.
[52] E.B. Nauman, D.Q. He, Nonlinear diffusion and phase separation, Chem. Eng. Sci. 56 (2001) 1999–2018.
[53] J.W. Cahn, C.M. Elliott, A. Novick-Cohen, The Cahn–Hilliard equation with a concentration dependent mobility: motion by minus the Laplacian of the mean curvature, European J. Appl. Math. 7 (1996) 287–301.
[54] C.M. Elliott, H. Garcke, On the Cahn–Hilliard equation with degenerate mobility, SIAM J. Math. Anal. 27 (1996) 404–423.

[55] F. Boyer, L. Chupin, P. Fabrie, Numerical study of viscoelastic mixtures through a Cahn–Hilliard flow model, Eur. J. Mech. B Fluids 23 (2004) 759–780.
[56] D. Kay, R. Welford, A multigrid finite element solver for the Cahn–Hilliard equation, J. Comput. Phys. 212 (2006) 288–304.
[57] H. Ding, P.D.M. Spelt, C. Shu, Diffuse interface model for incompressible two-phase flows with large density ratios, J. Comput. Phys. 226 (2007) 2078–2095.
[58] J. Kim, A numerical method for the Cahn–Hilliard equation with a variable mobility, Commun. Nonlinear Sci. Numer. Simul. 12 (2007) 1560–1571.
[59] H.G. Lee, J. Kim, A second-order accurate non-linear difference scheme for the N-component Cahn–Hilliard system, Physica A 387 (2008) 4787–4799.
[60] R. Toral, A. Chakrabarti, J.D. Gunton, Numerical study of the Cahn–Hilliard equation in three dimensions, Phys. Rev. Lett. 60 (1988) 2311–2314.
[61] D.J. Eyre, An unconditionally stable one-step scheme for gradient systems, Preprint, 1998.
[62] X. Feng, A. Prohl, Numerical analysis of the Cahn–Hilliard equation and approximation for the Hele–Shaw problem, Interfaces Free Bound. 7 (2005) 1–28.
[63] E.V.L. de Mello, O. Teixeira da Silveira Filho, Numerical study of the Cahn–Hilliard equation in one, two and three dimensions, Physica A 347 (2005) 429–443.
[64] H.D. Ceniceros, A.M. Roma, A nonstiff, adaptive mesh refinement-based method for the Cahn–Hilliard equation, J. Comput. Phys. 225 (2007) 1849–1862.
[65] W.M. Feng, P. Yu, S.Y. Hu, Z.K. Liu, Q. Du, L.Q. Chen, A Fourier spectral moving mesh method for the Cahn–Hilliard equation with elasticity, Commun. Comput. Phys. 5 (2009) 582–599.
[66] H.G. Lee, J. Kim, Accurate contact angle boundary conditions for the Cahn–Hilliard equations, Comput. & Fluids 44 (2011) 178–186.
[67] P. Yue, J.J. Feng, C. Liu, J. Shen, A diffuse-interface method for simulating two-phase flows of complex fluids, J. Fluid Mech. 515 (2004) 293–317.
[68] D. Jacqmin, Calculation of two-phase Navier–Stokes flows using phase-field modeling, J. Comput. Phys. 155 (1999) 96–127.
[69] J. Kloubek, Development of methods for surface free energy determination using contact angles of liquids on solids, Adv. Colloid Interface Sci. 38 (1992) 99–142.
[70] P.C. Philippi, K.K. Mattila, D.N. Siebert, L.O.E. dos Santos, L.A. Hegele Júnior, R. Surmas, Lattice-Boltzmann equations for describing segregation in non-ideal mixtures, J. Fluid Mech. 713 (2012) 564–587.
[71] F.H. Harlow, J.E. Welch, Numerical calculation of time-dependent viscous incompressible flow of fluid with free surface, Phys. Fluids 8 (1965) 2182–2189.
[72] H.G. Lee, K. Kim, J. Kim, On the long time simulation of the Rayleigh–Taylor instability, Internat. J. Numer. Methods Engrg. 85 (2011) 1633–1647.
[73] U. Trottenberg, C. Oosterlee, A. Schüller, Multigrid, Academic Press, London, 2001.
[74] S. Chandrasekhar, Hydrodynamic and Hydromagnetic Stability, Clarendon Press, Oxford, 1961.